aerospace

MDPI

Article

Hugoniot Relation for a Bow-Shaped Detonation Wave Generated in RP Laser Propulsion

Kenya Sugamura [1,*], Kyohei Kato [1], Kimiya Komurasaki [1], Hokuto Sekine [1], Yuma Itakura [1] and Hiroyuki Koizumi [2]

[1] Department of Aeronautics and Astronautics, The University of Tokyo, 7-3-1 Hongo, Bunkyo, Tokyo 113-8656, Japan
[2] Department of Advanced Energy, The University of Tokyo, 5-1-5 Kashiwa-no-ha, Kashiwa, Chiba 277-8561, Japan
* Correspondence: k.sugamura@al.t.u-tokyo.ac.jp

Abstract: Repetitive-pulsed (RP) laser propulsion is expected to replace chemical propulsion systems because it can reduce launch costs. A laser-supported detonation wave (LSD) plays an important role in the thrust-generation process of RP laser propulsion. The LSD propagation mechanism has been studied. Nevertheless, the LSD propagation velocity measured in an earlier study was lower than the Chapman–Jouguet (CJ) velocity, which meant that Hugoniot analysis produced no solution. The findings suggest that the radial flow from the central axis of LSD exerts some effects, but it has not been evaluated quantitatively. Two-dimensional axisymmetric computational fluid dynamics (CFD) analysis using the measured propagation velocity was performed for this study to evaluate effects of the radial flow of a bow-shaped LSD. Results show that the ratios of the radial flow of mass, momentum, and enthalpy from the central axis can be calculated, respectively, as 0.82, 0.13, and 0.17. Additionally, the measured propagation velocity of a bow-shaped LSD was shown to be higher than the CJ velocity calculated using the two-dimensional axisymmetric CFD reproducing the experiment conditions.

Keywords: computational fluid dynamics; laser discharge; laser supported detonation; plasma physics; shock wave

Citation: Sugamura, K.; Kato, K.; Komurasaki, K.; Sekine, H.; Itakura, Y.; Koizumi, H. Hugoniot Relation for a Bow-Shaped Detonation Wave Generated in RP Laser Propulsion. *Aerospace* **2023**, *10*, 102. https://doi.org/10.3390/aerospace10020102

Academic Editor: John Sinko

Received: 26 December 2022
Revised: 16 January 2023
Accepted: 18 January 2023
Published: 19 January 2023

1. Introduction

Laser propulsion has been proposed as an alternative to chemical propulsion for space transportation systems [1]. One system, repetitive-pulsed (RP) laser propulsion, can reduce launch costs because its energy is provided by a laser base on a ground. Moreover, it uses the atmosphere as a propellant, thereby achieving a high payload ratio [2]. In the RP laser propulsion thrust-generation process, a laser-supported detonation wave (LSD) plays an important role. The LSD phenomenon resembles chemical detonation, but plasma absorbs laser energy. The resultant shock wave propagates at supersonic velocity. In the LSD state, the laser energy is converted efficiently to pressure, but as the laser intensity decreases, the LSD state becomes a laser-supported combustion wave (LSC), with the gas heated isobarically [3–5].

The LSD propagation velocity is an important parameter because the heating rate in the LSD state depends on the velocity. Zeldovich and Raizer suggested that the propagation velocity could be the Chapman–Jouguet (CJ) velocity if the effectiveness of other ionization mechanisms is less than that of ionization by a shock wave [3,6]. Then, it can be inferred that LSD has a Zeldovich-von Neumann-Döring (ZND) structure similar to that of chemical detonation. The CJ velocity for LSD is written as a function of the laser intensity. They also suggested that the propagation velocity can be higher than the CJ velocity if the effectiveness of other ionization mechanisms is dominant. The LSD propagation mechanism has not been demonstrated experimentally with clarity.

Therefore, Matsui [7] accurately measured the LSD propagation velocity to produce an appropriate LSD propagation model. However, the measured propagation velocity on

the central axis of LSD was lower than the CJ velocity, indicating that Hugoniot analysis had no solution. The effects of the radial flow from the central axis of LSD apparently produced these results. Because the LSD wavefront observed in the experiment has had a three-dimensional extent, it is considered that radial flow from the central axis exists such that one-dimensional analysis cannot be used. Takeda et al. [8] reported that a solution to the Hugoniot analysis can exist, assuming more than 80% of the enthalpy flowed out from the central axis, but the radial flow effects must be investigated in greater detail.

For this study, two-dimensional axisymmetric computational fluid dynamics (CFD) analyses reproducing the experiment conditions were applied to evaluate the effects of the radial flow from the central axis of a bow-shaped LSD. The findings revealed that mass, momentum, and enthalpy flow out from the central axis. Additionally, the results demonstrated that the CJ velocity calculated using CFD is lower than the measured propagation velocity of a bow-shaped LSD.

2. Numerical Methods

2.1. Numerical Models

2.1.1. Analytical Model Reproducing the Experiment Conditions

A bow-shaped LSD observed from experiments was simulated numerically. For the experiments, a transversely excited atmospheric pressure (TEA) CO_2 laser (10 J/pulse maximum energy, 10.6 μm wavelength) was used. It had a history of laser power and cumulative energy, as shown in Figure 1. The laser cross section has the shape of a 30 × 30 mm square, with different transverse modes in the horizontal and vertical directions. Therefore, the beam was focused by two mirrors, as shown in Figure 2. An aluminum target was placed at the focal point. Then an LSD was generated on it. Numerical calculations reproduced the experiment conditions using these characteristics of the laser and focusing optics. Additionally, the propagation velocity and shape of ionization wavefront and the local laser intensity were given as input parameters based on the measurements. The details will be described later.

2.1.2. Ionization Wavefront Propagation Velocity

For this calculation, the propagation velocity on the central axis of the ionization wavefront, U_{ioniz}, was given as the measured value. For experimentation, Matsui [7] measured U_{ioniz} at each laser intensity using the system presented above. That study showed that the relation between U_{ioniz} and the laser intensity on the central axis S_{peak} can be written as:

$$U_{\mathrm{ioniz}} = \alpha {S_{\mathrm{peak}}}^{\beta}. \quad (1)$$

Here α and β, respectively, denote the coefficients of fitting. They are shown to vary at S = 500 GW/m^2, as portrayed in Figure 3.

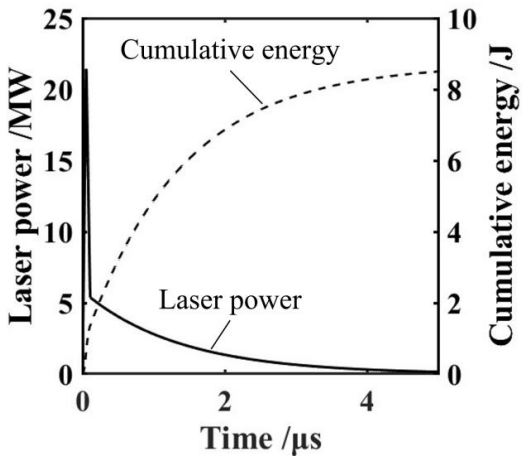

Figure 1. History of laser power and cumulative energy of the TEA CO_2 laser used for experimentation.

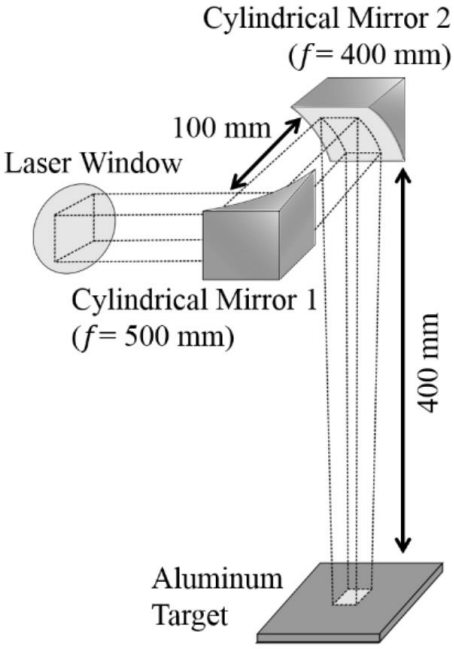

Figure 2. Schematic showing the focusing optics used for experimentation.

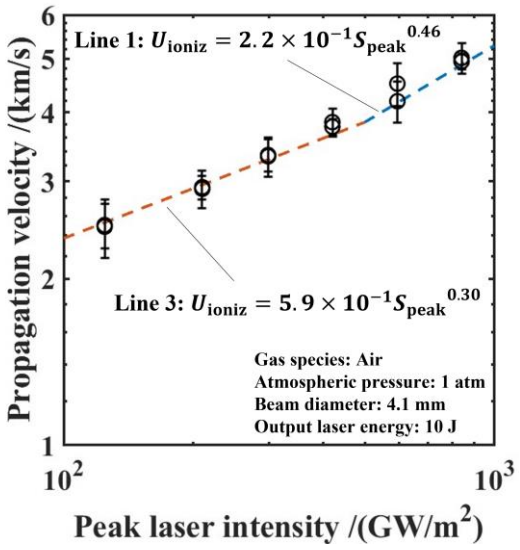

Figure 3. Relation between the laser intensity and measured propagation velocity on the central axis [7].

2.1.3. Ionization Wavefront Shape

The laser used for the experiment had a profile with a peak at the center, defined as a "Gaussian" and "Top-hat" profile, as shown in Figure 4a. The laser intensity varied depending on the radial position. For that reason, the bow-shaped ionization wavefront shown in Figure 4b was formed. For this calculation, the ionization wavefront shape was given by these experimentally obtained results.

2.1.4. Laser Intensity Calculation

The two-dimensional distribution of laser intensity is calculable as

$$S(x, y, t) = \frac{R_{\text{peak}} P(t)}{4 W_{G0} W_{T0}} G(x) T(y). \tag{2}$$

R_{peak} represents the ratio of the peak laser intensity to the average laser intensity, 2.26, and $P(t)$ denotes the laser power shown in Figure 1. Additionally, W_{G0} and W_{T0} are the

beam radii at the focal point for the respective directions shown in Figure 4a. $G(x)$ and $T(y)$, respectively, represent Gaussian and Top-hat profiles for each axial direction shown in Figure 4a. The two-dimensional distribution of the profile is calculable by multiplying them as shown in Figure 5a. Furthermore, x and y were defined as in Figure 5a.

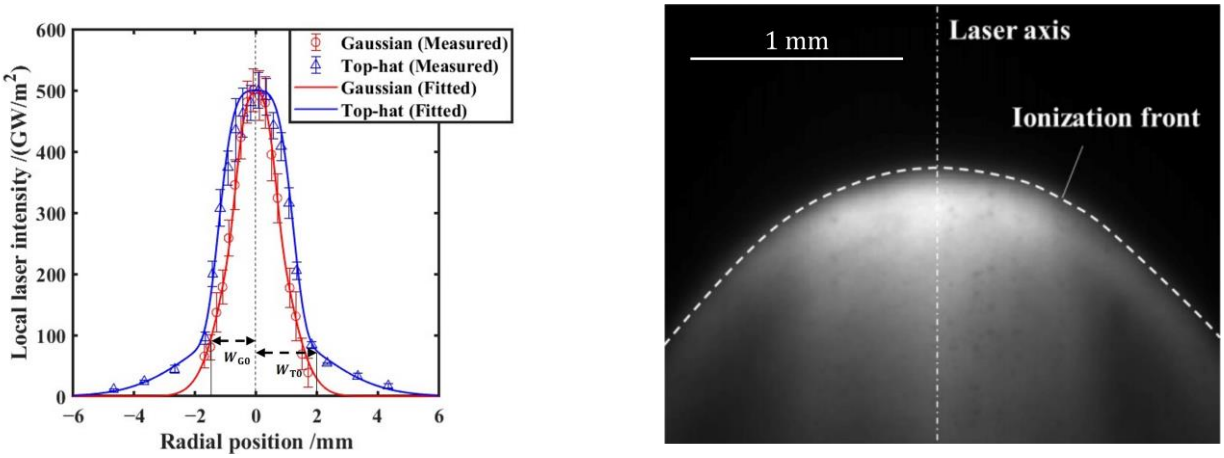

Figure 4. (**a**) Measured beam profile at the focal point in each axial direction [7] and (**b**) self-emission photograph of a bow-shaped ionization wavefront in the Gaussian direction [7].

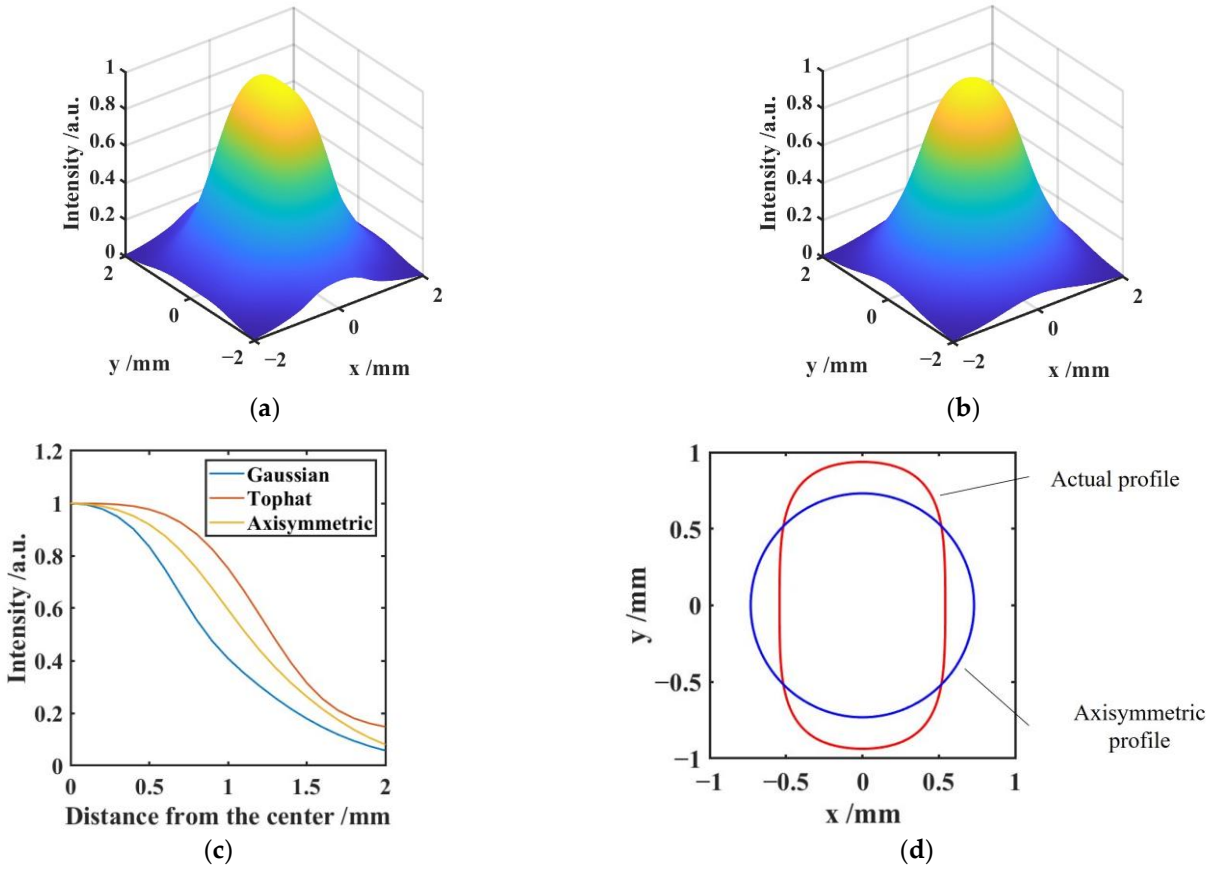

Figure 5. Spatial distribution of (**a**) actual profile and (**b**) axisymmetric profile. Here, x and y, respectively, represent the Gaussian and Top-hat directions. (**c**) Variation of each profile with respect to distance from the center. (**d**) Cross-sectional shape of each profile at intensity of 0.8.

For this calculation, the beam profile was assumed to be axisymmetric. Therefore, the laser intensity at each position r can be presented as shown below.

$$S(r,t) = \frac{R_{\text{peak}}P(t)}{4W_{G0}W_{T0}}G'(r)T'(r). \tag{3}$$

Here $G'(r)$ and $T'(r)$ represent the profile assumed to be axisymmetric. Its distribution is calculable as shown in Figure 5b. The total laser energy given with this assumption was the same as that of the actual profile. The CFD results were validated by comparing the measured and calculated pressure histories on the bottom wall, which were sensitive to the total laser energy and insensitive to the profiles of laser intensities.

2.2. Governing Equations

In this analysis, Euler equations were adopted because the boundary layer thickness was estimated to be at most 0.01 of the laser diameter. The ionization reactions were not considered because the shock Mach number was at most nine during the time period focused on in this study. Dissociation reactions were also neglected for simplicity in this calculation.

The following two-dimensional axisymmetric Euler equations were used:

$$\frac{\partial Q}{\partial t} + \frac{\partial E}{\partial z} + \frac{\partial F}{\partial r} + \frac{H}{r} = S, \tag{4}$$

$$\begin{aligned} Q&= \begin{pmatrix} \rho \\ \rho u \\ \rho v \\ \rho e \end{pmatrix}, E = \begin{pmatrix} \rho u \\ p + \rho u^2 \\ \rho uv \\ (\rho e + p)u \end{pmatrix}, F = \begin{pmatrix} \rho v \\ \rho uv \\ p + \rho v^2 \\ (\rho e + p)v \end{pmatrix} \\ H&= \begin{pmatrix} \rho v \\ \rho uv \\ \rho v^2 \\ (\rho e + p)v \end{pmatrix}, S = \begin{pmatrix} 0 \\ 0 \\ 0 \\ W \end{pmatrix} \end{aligned} \tag{5}$$

In those equations, w in the source term represents the heat input by laser through inverse bremsstrahlung. For this calculation, thermal equilibrium was assumed between heavy particles and electrons. The laser energy was added directly to the heavy particles.

Heating by laser occurs only inside the absorbing layer of the laser. Additionally, w can be written as:

$$w(z,r,t) = \begin{cases} \eta \frac{S(r,t)}{l_{\text{abs}}} & (z_{\text{ioniz}} - l_{\text{abs}} \leq z \leq z_{\text{ioniz}}) \\ 0 & (\text{otherwise}) \end{cases}. \tag{6}$$

In Equation (6), uniform heating in the laser absorbing layer is assumed. Furthermore, z_{ioniz} represents the z-axis position of the ionization wavefront at each position r, calculated as:

$$z_{\text{ioniz}}(r,t) = z_{\text{ioniz},0}(r) + \int_0^t U_{\text{ioniz}} dt. \tag{7}$$

Here, $z_{\text{ioniz},0}$ stands for the initial position of the ionization wavefront defined as shown in the next section. l_{abs} represents the laser-absorbing layer length, which was set as 0.2 mm based on a measured value from an earlier study [4]. By introducing heating efficiency η, losses such as energy used for dissociation and ionization and losses caused by radiation were considered. Although η is regarded as varying in time and space, it was assumed to be constant in this calculation. The value of η was determined using the measured value of the blast wave conversion efficiency. The laser energy absorbed in the LSD state is converted into the internal and kinetic energy of the blast wave. Additionally, the ratio of the input laser energy to the blast wave energy is defined as the blast wave conversion efficiency η_{bw} [9]. Actually, η_{bw} in the CFD calculation results was obtained by

calculating the propagation history of shock wave in the axial and radial directions after laser irradiation and using the same method as that used in an earlier study [9], which employed the Sedov–Taylor self-similar solution [3,10,11]. The shock wavefront position was defined as the position in which the density took the average of the maximum and atmospheric density. Consequently, η was set to 0.49 as a value that reproduced $\eta_{bw} = 0.41$ obtained in an earlier study [8]. These calculation results are presented in Figure 6. Because LSD ended at approximately 2.3 μs, the fitting was applied after 5 μs, when the adiabatic expansion was obtained. In this figure, the calculated propagation histories of the shock wavefront and ionization wavefront are shown only in the fitting range. Moreover, it is apparent that they are well approximated by the self-similar solution. Laser heating was applied only during LSD duration. Additionally, the threshold laser intensity for LSD termination was set as 170 GW/m^2 based on the results of experimentation.

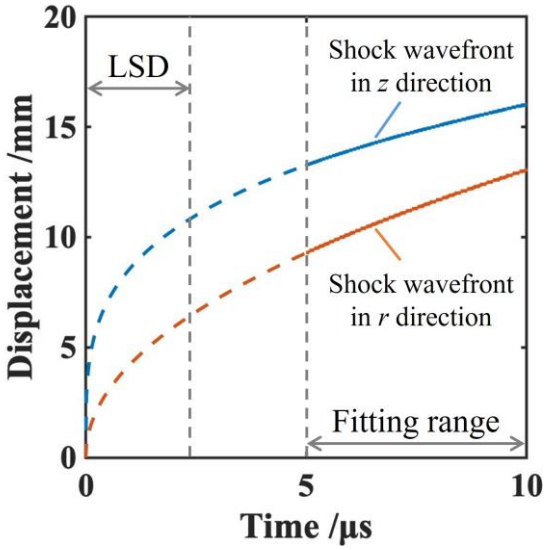

Figure 6. Calculation results and fitting curves of shock wavefront propagation history in the z and r directions. Solid lines represent calculated values. Dashed lines represent fitting curves.

2.3. Calculation Conditions

Initial conditions were given as a standard atmosphere, which was treated as a calorimetrically perfect gas. Therefore, the specific heat ratio was set as 1.4. Because the laser heating was given by Equation (6), the initial plasma did not have to be considered. The input energy was set as 7.5 J, which was equal to the input energy in the experiments as described later. The propagation velocity of the ionization wavefront is calculated using Equation (1). However, in those experiments, the ionization wavefront propagated faster than U_{ioniz} calculated using Equation (1) immediately after initiation of the laser irradiation. The reason is regarded as the dominance of breakdown wave [6] at that time. Therefore, for this calculation, this very high velocity was expressed by giving the initial position of the ionization wavefront. For this calculation, the initial position of the ionization wavefront on the central axis was set as 1.4 mm in reference to the measured values. That at each radial position r, $z_{ioniz,0}(r)$ was set considering the bow-shaped wavefront described in Section 2.1.3.

The boundary conditions were set as explained hereinafter. At the central axis, axisymmetric conditions were chosen. At the bottom, slip conditions were applied because the boundary expressed the Al target used in the experiments. The runoff conditions were chosen at other boundaries.

The spatial accuracy was set to the third order using the MUSCL method. The minmod function was used as the flux-limiting function. The fractional time step was chosen to ensure second-order accuracy in time. The cell widths were set as $dz = 0.02$ mm, $dr = 0.1$ mm, and CFL = 0.5. Grid convergence was confirmed using calculated results of the distance between the shock wavefront and the ionization wavefront.

3. CFD Code Validation Based on Pressure History Calculated and Measured Values

3.1. Validation Methods

To validate the CFD code developed for this study, the pressure history on the bottom wall was measured by experimentation. It was then compared with that calculated using the CFD code.

For experimentation, an LSD was generated using the focusing optics in Figure 2. As shown in Figure 7, a pressure sensor (603B; Kistler Japan Co. Ltd., Kanagawa, Japan) was installed at the focal point so that its central axis was aligned with the laser axis. The pressure sensor output was amplified using a charge amplifier (5011B; Kistler Japan Co. Ltd., Kanagawa, Japan). Additionally, the output history was obtained using an oscilloscope. The pressure sensor surface was covered with thin grease and aluminum foil to avoid thermal shock effects [12].

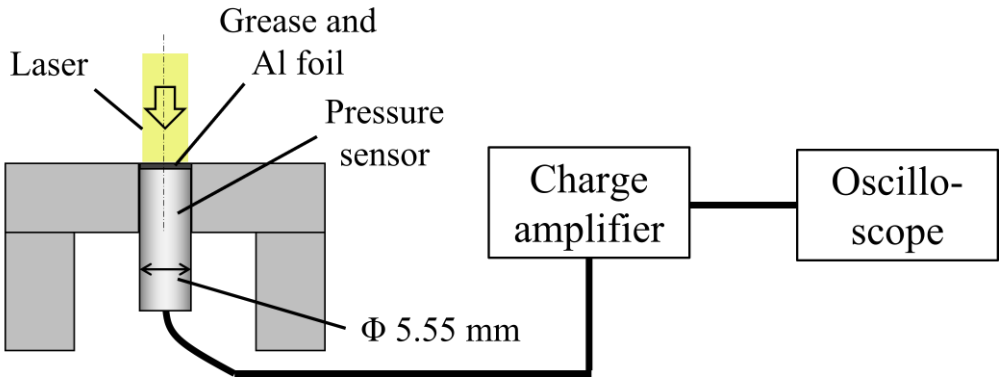

Figure 7. Experiment apparatus used for pressure measurements.

The pressure history in CFD was obtained by calculating the average value of the pressure applied to the pressure sensor using a following equation:

$$p_{\text{sensor}}(t) = \frac{\int_0^{R_{\text{sensor}}} p_{\text{wall}}(r,t) 2\pi r \, dr}{\pi {R_{\text{sensor}}}^2}. \tag{8}$$

Therein, R_{sensor} is the radius of the pressure-sensing surface of the pressure sensor, which is 2.775 mm.

3.2. Validation Results

For experimentation, the laser energy measured using the energy meter (QE50 LP-H-MB; Gentec-EO Inc., Quebec City, QC, Canada) was 7.5 ± 0.6 J. The output laser energy is shown in Figure 2, but the energy was attenuated because of the reflectivity of the focusing mirrors. Figure 8a shows the measured and calculated pressure histories on the bottom wall. The calculated value showed a steep rise. The waveform differed from the measured value. The reason for this result is considered to be that the measured pressure was filtered because of the frequency band of the charge amplifier and the rise time of the pressure sensor. The calculated pressure history was filtered and compared with the measured pressure history. For this process, the filter applied by the charge amplifier was reproduced using a low pass filter, as shown in Figure 9. Results indicate that the calculated pressure history processed by the filter showed the same shape as the measured pressure history, as shown in Figure 8b. Table 1 presents a comparison of the peak pressure and plateau pressure, which is defined as the pressure settling to a constant value of the calculated and measured pressure history. The plateau pressure was calculated as the average value of the pressure history after 6 μs. The findings agreed within the range of error of measured values. The CFD code developed for this study was validated.

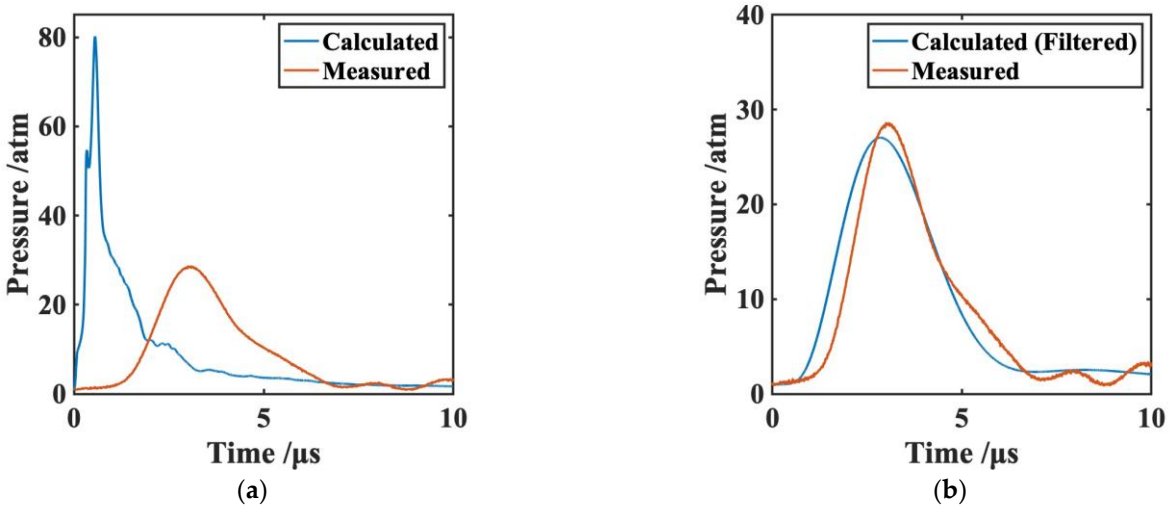

Figure 8. Comparison of pressure histories as: (**a**) calculated and measured and as (**b**) calculated using the filter and measured.

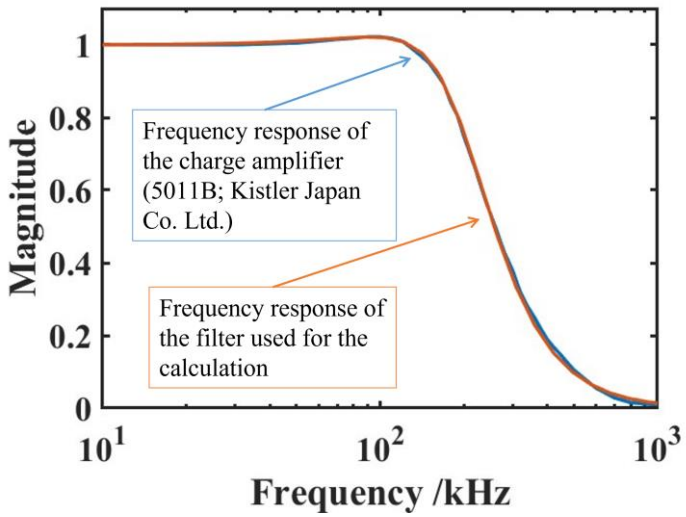

Figure 9. Frequency responses of the charge amplifier and the filter used for calculations.

Table 1. Peak pressures and plateau pressures of pressure histories as measured and calculated using the filter.

	Peak Pressure/atm	Plateau Pressure/atm
Calculated value	27.04	2.43
Measured value	28.57 ± 2.21	2.27 ± 0.44

4. Calculation Results by Two-Dimensional Axisymmetric CFD

4.1. Calculation Results of the Propagation History of LSD

To confirm the validity of the calculation results, the propagation histories of the shock and the ionization wavefronts on the central axis were obtained. They are shown in Figure 10. The shock and the ionization wavefronts propagated at approximately equal velocities, so that the probable LSD state was obtained. Immediately after the beginning of the laser irradiation, the wavefront distance was not constant, but a steady state was obtained after 1 μs. The reason for this result is that the laser power history had a spike with a large change. The ionization wavefront was about 0.2 mm behind the shock wavefront in a steady state. This result suggests that the main region heated by a laser is located

some distance behind the shock wavefront. Because plasma was shown to exist at the shock wavefront [13], prior heating by the seed electron must be considered for more detailed discussion of the LSD structure. However, the electron number density at the shock wavefront is not so high that most of a laser is absorbed in the main heating region behind the shock wavefront. As described in the next section, analysis of the central axis was performed in a steady state.

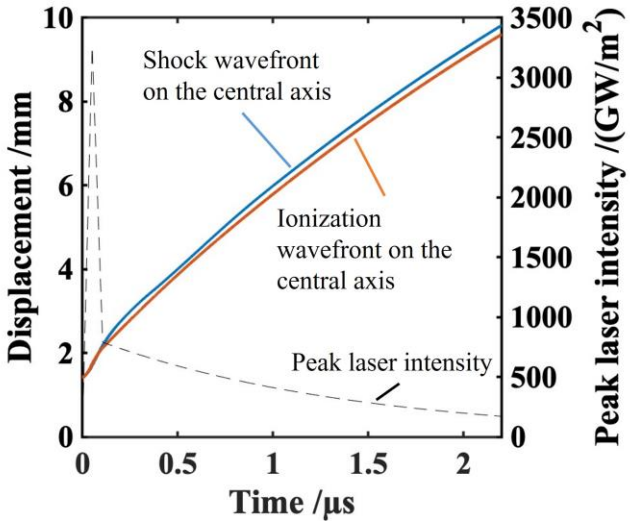

Figure 10. Propagation history of the shock and ionization wavefronts.

4.2. Evaluating Effects of Radial Flow from the Central Axis of LSD

Conservation equations forward and backward LSD considering radial flow from the central axis of LSD can be written as:

$$\rho_1 u_1 \cdot (1 - \eta_{\text{mass}}) = \rho_2 u_2, \tag{9}$$

$$p_1 + \rho_1 u_1^2 \cdot (1 - \eta_{\text{momentum}}) = p_2 + \rho_2 u_2^2, \tag{10}$$

$$h_1 + \frac{1}{2}u_1^2 + \frac{\eta S_{\text{peak}}}{\rho_1 u_1} \cdot \left(1 - \eta_{\text{enthalpy}}\right) = \frac{\rho_2 u_2}{\rho_1 u_1}\left(h_2 + \frac{1}{2}u_2^2\right). \tag{11}$$

Subscript 1 represents the initial state in front of the wavefront, defined as state 1; subscript 2 represents the rear of the heating region, defined as state 2. Therein, η_{mass}, η_{momentum}, and η_{enthalpy}, respectively, represent the effects of the radial flow of mass, momentum, and enthalpy from the central axis, defined as the ratio of the amount of the radial flow to the largest term on the left side for each equation.

The results of CFD calculations provided each physical quantity in states 1 and 2. These were used to calculate η_{mass}, η_{momentum}, and η_{enthalpy}. Figure 11 presents the results of calculations. η_{momentum} and η_{enthalpy} are moving averaged values because of oscillations attributable to the cell width. In a steady state, they were almost constant irrespective of the laser intensity. The average values were calculated as shown in Table 2. As the peak laser intensity approached the threshold value for LSD termination, the amounts of the radial flow of mass, momentum, and enthalpy tended to increase because the off-axis heating rate decreased as the off-axis LSD terminated. More radial flow occurred from the central axis to drive the off-axis blast wave.

As shown in Figure 11, the relation between the laser intensity and the ratio of the radial flow was investigated for different input energies. These values were obtained by the calculation with the same conditions except for the input energy. In the range of laser intensities shown in Figure 11, the ratio of the radial flow was almost the same for conditions above 7.5 J. For 5 J, the values were not constant at higher laser intensities because a steady state was not achieved at these laser intensities. However, at lower laser

intensities, a steady state was achieved, and the values became almost constant. These values were consistent with the values obtained for conditions above 7.5 J. This result indicates that the ratios of the radial flow of mass, momentum, and enthalpy in a steady state are independent of the input energy.

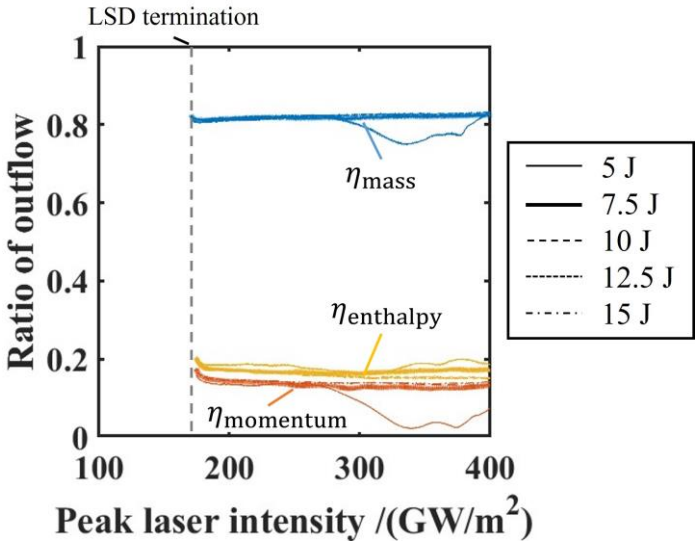

Figure 11. Variation of the ratio of the radial flow of mass, momentum, and enthalpy according to the peak laser intensity for different input energies.

Table 2. Average values in the range of 200–400 GW/m^2 of η_{mass}, η_{momentum}, and η_{enthalpy} in a steady state.

	η_{mass}	$\eta_{momentum}$	$\eta_{enthalpy}$
Average value	0.82	0.13	0.17

4.3. Hugoniot Relation Considering Radial Flow from the LSD Central Axis

The Rayleigh line and Hugoniot curve were derived using Equations (9)–(11). The Rayleigh line can be written as

$$\frac{p_2}{p_1} = 1 + \left\{ (1 - \eta_{\mathrm{momentum}}) - (1 - \eta_{\mathrm{mass}})^2 \frac{v_2}{v_1} \right\} \frac{\rho_1 {u_1}^2}{p_1}. \tag{12}$$

Here v_1 and v_2, respectively, represent the specific volume at state 1 and state 2. With the assumption of $p_1 \ll p_2$ [3], the Hugoniot curve can be written as shown below.

$$p_2 = \left[\frac{2{\rho_1}^{\frac{1}{2}} \sqrt{(1 - \eta_{\mathrm{momentum}}) - (1 - \eta_{\mathrm{mass}})^2 \frac{v_2}{v_1}} \left(1 - \eta_{\mathrm{enthalpy}}\right) \eta S_{\mathrm{peak}}}{(1 - \eta_{\mathrm{mass}}) \frac{2\gamma}{\gamma - 1} \frac{v_2}{v_1} - \frac{1 - (1 - \eta_{\mathrm{mass}})^3 \left(\frac{v_2}{v_1}\right)^2}{(1 - \eta_{\mathrm{momentum}}) - (1 - \eta_{\mathrm{mass}})^2 \frac{v_2}{v_1}}} \right]^{\frac{2}{3}}. \tag{13}$$

In that equation, γ represents the specific heat ratio. Figure 12 shows the results of drawing these on p—v diagram for each laser intensity. The figure also includes changes to the p—v diagram of the CFD calculation results. For each laser intensity, the Rayleigh line and Hugoniot curve had a cross point, which is consistent with state 2 of the CFD calculation results.

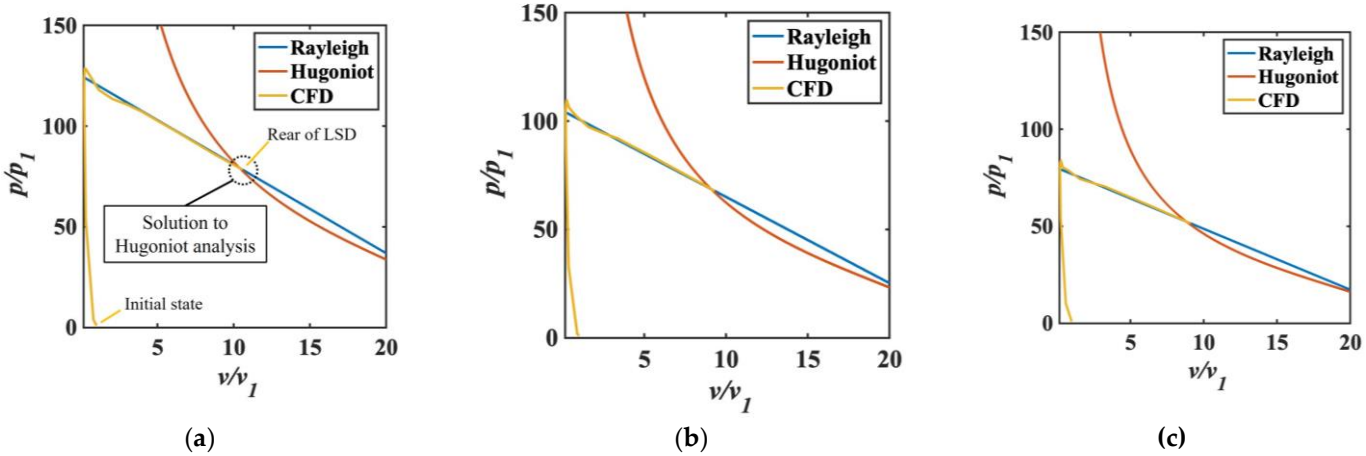

Figure 12. p—v diagram for: (**a**) $S_{\text{peak}} = 400$ GW/m^2, (**b**) $S_{\text{peak}} = 300$ GW/m^2, and (**c**) $S_{\text{peak}} = 200$ GW/m^2. The changes on the p—v diagram of the CFD calculation results are written from state 1 to state 2.

These results suggest that the effects of the radial flow from the central axis of LSD are significant in a bow-shaped LSD. Results show that the mass and momentum also flow out in the radial direction, but for an earlier study, it was assumed that only enthalpy flowed out [8]. In particular, the radial flow of mass was large, which results in a small density behind LSD. A solution to Hugoniot analysis was obtained at $v/v_1 > 1$.

5. Discussion

5.1. Differences in the Radial Flows of Mass, Momentum, and Enthalpy

As described in the preceding section, the mass, momentum, and enthalpy flowed out from the central axis. η_{mass} was about five times as large as η_{momentum} and η_{enthalpy}, presumably because the temperature is comparably low in the region between the shock wavefront and the ionization wavefront where most of the mass flows out. Figure 13 shows the spatial distributions of density, axial velocity, and total enthalpy in shock wave fixed coordinates in a steady state. As might be apparent from Figure 13a, the high-density region is in front of the heating region, where most of the mass should flow out. The density becomes small inside the heating region. However, Figure 13b,c show that the axial velocity and total enthalpy are small in the high-density region in front of the heating region. They become large inside the heating region and behind the heating region. However, because little mass flows out from these regions, neither momentum nor enthalpy flows out. For these reasons, only the radial flow of mass was large.

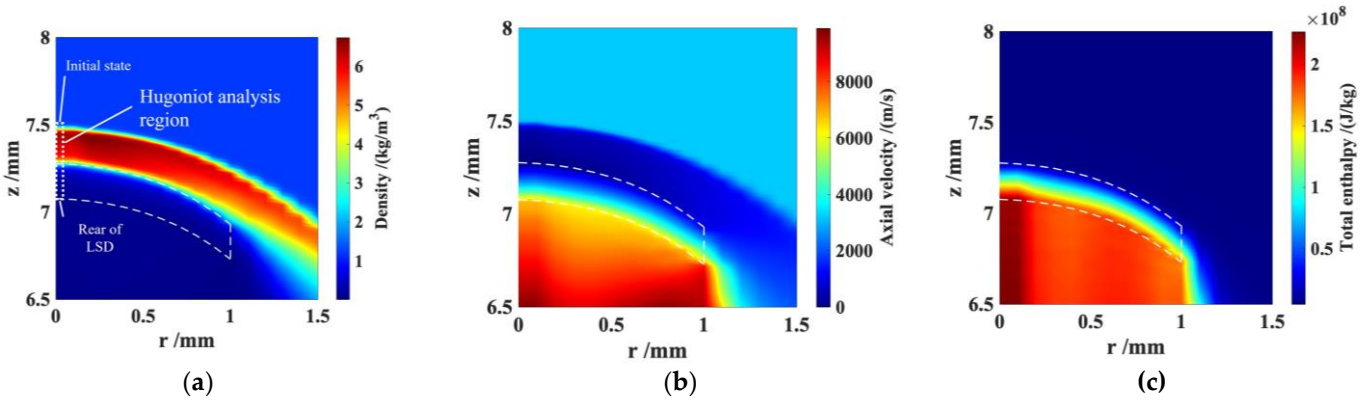

Figure 13. Spatial distribution of: (**a**) density, (**b**) axial velocity, and (**c**) total enthalpy in shock wave fixed coordinates at $S_{\text{peak}} = 300$ GW/m^2.

In this calculation, η_{mass}, η_{momentum}, and η_{enthalpy} were estimated as shown in Figure 11 and Table 2, and the radial mass flow is mainly induced in the layer between the shock wavefront and the heating region. According to the flow similarity with the shock layer formed ahead of a blunt body, η_{mass}, η_{momentum}, and η_{enthalpy} will increase with a decrease in the radius of curvature of the ionization wavefront.

5.2. Comparison of CJ Velocity Calculated Using the Two-Dimensional Axisymmetric CFD with the Measured Propagation Velocity

The CJ velocity was derived for the condition in which the Rayleigh line touches the Hugoniot curve [14]. Using Equations (12) and (13), the CJ velocity can be derived while considering the radial flow effects as shown below.

$$U_{\mathrm{CJ}} = \left\{ \frac{(1-\eta_{\mathrm{mass}})\left(1-\eta_{\mathrm{enthalpy}}\right)}{\gamma^2(1-\eta_{\mathrm{momentum}})^2-(1-\eta_{\mathrm{mass}})(\gamma^2-1)} \right\}^{\frac{1}{3}} \cdot \left\{ 2\left(\gamma^2-1\right)\frac{\eta S_{\mathrm{peak}}}{\rho_1} \right\}^{\frac{1}{3}}. \quad (14)$$

In this equation, the latter part represents the one-dimensional CJ velocity. The part representing the effects of the radial flow is multiplied. This part was calculated as 0.48 using the average value of the ratio of the radial flow shown in Table 2. Therefore, the CJ velocity becomes lower given the effects of the radial flow. Results show that the CJ velocity also decreases in a planar curved chemical detonation [15–17], but only by a factor of about 0.8 [17]. Results obtained from this calculation indicate singularity of the central axis.

Figure 14a presents a comparison of propagation velocity. In this figure, plots of measured propagation velocity are identical to those in Figure 3, which were measured by Matsui [7]. As might be apparent from this figure, CJ velocity calculated using the CFD is lower than the measured propagation velocity. The line expressing U_{CJ} is overlapped by some of the error bars. For that reason, more accurate measurements are needed. However, U_{CJ} is probably lower than the measured propagation velocity at almost all laser intensities.

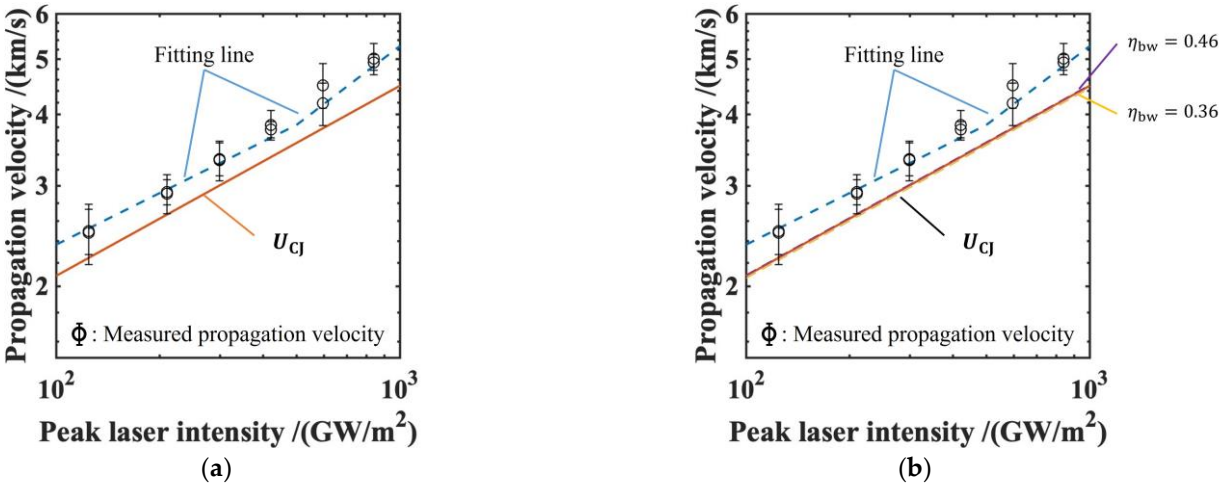

Figure 14. (**a**) Measured propagation velocity and CJ velocity considering the effects of radial flow and (**b**) considering the error in η_{bw}.

For this calculation, heating efficiency η in Equation (6) was given for the measured blast wave conversion efficiency as η_{bw}. It included an experimental error of 0.05. Therefore, the calculation was also performed with values incorporating the experimental error. Additionally, U_{CJ} was calculated with each η_{bw}. These results are presented in Figure 14b. Then they are almost identical. Therefore, U_{CJ} is probably lower than the measured propagation velocity, even considering error attributable to experimentation.

In the Hugoniot analysis using η_{mass}, η_{momentum}, and η_{enthalpy} shown in Table 2, the CJ velocity was decreased by 0.48 from the one-dimensional prediction, and it will decrease with a further decrease in the radius of curvature of the ionization wavefront.

6. Conclusions

As described herein, two-dimensional axisymmetric CFD analysis was performed to evaluate the effects of the radial flow from the central axis of a bow-shaped LSD. The findings indicate that radial flows of mass, momentum, and enthalpy exist. The ratios of the radial flow of mass, momentum, and enthalpy from the central axis were calculated, respectively, as 0.82, 0.13, and 0.17 as average values in a steady state. The radial flow of mass was especially large because the region in which most of mass flows out precedes the region where momentum and enthalpy increase. Additionally, by considering the radial flow, a solution to Hugoniot analysis exists even at the measured propagation velocity. Furthermore, results showed that the measured propagation velocity of a bow-shaped LSD is higher than the CJ velocity calculated using the two-dimensional axisymmetric CFD, reproducing the experiment conditions, which is about 0.48 times the theoretical one-dimensional CJ velocity.

Author Contributions: Conceptualization, K.S. and K.K. (Kimiya Komurasaki); methodology, K.S., K.K. (Kyohei Kato) and K.K. (Kimiya Komurasaki); software, K.S.; validation, K.S. and K.K. (Kyohei Kato); investigation, K.S., K.K. (Kyohei Kato) and Y.I.; resources, K.K. (Kimiya Komurasaki) and H.S.; data curation, K.S., K.K. (Kyohei Kato) and Y.I.; writing – original draft, K.S.; writing – review & editing, K.K. (Kyohei Kato), K.K. (Kimiya Komurasaki), H.S., Y.I. and H.K.; visualization, K.S.; supervision, K.K. (Kimiya Komurasaki), H.S. and H.K.; funding acquisition, K.K. (Kimiya Komurasaki) All authors have read and agreed to the published version of the manuscript.

Funding: This research was funded by JSPS Grant-in-Aid for Scientific Research no. JP20H02344.

Data Availability Statement: The data presented in this study are available on request from the corresponding author. The data are not publicly available due to privacy restrictions.

Conflicts of Interest: The authors declare no conflict of interest.

References

1. Kantrowitz, A. Laser Propulsion. *Astronaut. Aeronaut.* **1971**, *10*, 74.
2. Katsurayama, H.; Komurasaki, K.; Arakawa, Y. Feasibility for a Single-Stage-to-Orbit Launch to a Geosynchronous Transfer Orbit by Pulse Laser Propulsion. *J. Jpn. Soc. Aeronaut. Space Sci.* **2006**, *54*, 63–70.
3. Zel'dovich, Y.B.; Raizer, Y.P. *Physics of Shockwaves and High-Temperature Hydrodynamic Phenomena*; Dover: New York, NY, USA, 2002; pp. 338–348.
4. Shimamura, K.; Komurasaki, K.; Ofosu, J.A.; Koizumi, H. Precursor Ionization and Propagation Velocity of a Laser-Absorption Wave in 1.053 and 10.6-µm Wavelength Laser Radiation. *IEEE Trans. Plasma Sci.* **2014**, *42*, 3121–3128. [CrossRef]
5. Shiraishi, H.; Fujiwara, T. CFD Analysis on Unsteady Propagation of 1-Dimensional Laser-Supported Detonation Wave Using a 2-Temperature Model. *J. Jpn. Soc. Aeronaut. Space Sci.* **1998**, *46*, 607–613.
6. Raizer, Y.P. Heating of a gas by a powerful light pulse. *Sov. Phys. JETP* **1965**, *21*, 1009–1017.
7. Matsui, K. Study for Laser Parameters Determine the Propagation Velocity and the Wavefront Shape of Laser-Supported Detonation Wave. Ph.D. Thesis, The University of Tokyo, Tokyo, Japan, 2020.
8. Takeda, R.; Kanda, K.; Matsui, K.; Komurasaki, K.; Koizumi, H. Hugoniot Analysis of Laser Supported Detonation Using Measured Blast Wave Energy Efficiency. *J. IAPS* **2020**, *28*, 34–40.
9. Wang, B.; Komurasaki, K.; Yamaguchi, T.; Shimamura, K.; Arakawa, Y. Energy conversion in a glass-laser-induced blast wave in air. *J. Appl. Phys.* **2010**, *108*, 124911. [CrossRef]
10. Sedov, L.I. *Similarity and Dimensional Methods in Mechanics*; Academic Press: New York, NY, USA, 1959.
11. Kinney, G.F. *Explosive Shocks in Air*; Macmillan: New York, NY, USA, 1962.
12. Krause, T.; Meier, M.; Brunzendorf, J. Influence of thermal shock of piezoelectric pressure sensors on the measurement of explosion pressures. *J. Loss Prev. Process Ind.* **2021**, *71*, 104523. [CrossRef]
13. Shimamura, K.; Hatai, K.; Kawamura, K.; Fukui, A.; Fukuda, A.; Wang, B.; Yamaguchi, T.; Komurasaki, K.; Arakawa, Y. Structure Analysis of Laser Supported Detonation Waves by Two-Wavelength Mach–Zehnder Interferometer. *J. Jpn. Soc. Aeronaut. Space Sci.* **2010**, *58*, 323–329.
14. Lee, J.H.S. *The Detonation Phenomenon*; Cambridge University Press: New York, NY, USA, 2008.

15. Maeda, S.; Sumiya, S.; Kasahara, J.; Matsuo, A. Initiation and sustaining mechanisms of stabilized Oblique Detonation Waves around projectiles. *Proc. Combust. Inst.* **2013**, *34*, 1973–1980. [CrossRef]
16. Kudo, Y.; Nagura, Y.; Kasahara, J.; Sasamoto, Y.; Matsuo, A. Oblique detonation waves stabilized in rectangular-cross-section bent tubes. *Proc. Combust. Inst.* **2011**, *33*, 2319–2326. [CrossRef]
17. Nakayama, H.; Kasahara, J.; Matsuo, A.; Funaki, I. Front shock behavior of stable curved detonation waves in rectangular-cross-section curved channels. *Proc. Combust. Inst.* **2013**, *34*, 1939–1947. [CrossRef]